Creating exact multipolar fields with azimuthally modulated rf cavities

L. M. Wroe* and S. L. Sheehy†
Department of Physics, University of Oxford, OX1 3RH, United Kingdom

R. J. Apsimon
Engineering Department, Lancaster University, LA1 4YW, United Kingdom,
and Cockcroft Institute, Daresbury Laboratory, Warrington, WA4 4AD, United Kingdom

(Received 10 November 2021; accepted 13 May 2022; published 10 June 2022; corrected 16 June 2022)

Radio-frequency cavities used in modern particle accelerators operate in TM_{m10}-like modes composed of a single, dominant multipole of order m; $m = 0$ modes are used for the longitudinal acceleration of a particle beam and $m \neq 0$ modes for controlling transverse beam dynamics. The practical design of the latter, however, can be complex and require extensive analysis through the iteration of both approximate mathematical models and computationally expensive simulations to optimize the performance of the structure. In this paper we present a new, systematic method for designing azimuthally modulated rf cavities that support modes composed of any number and magnitude of user-specified transverse multipoles, either with or without a longitudinally accelerating component. Two case studies are presented of rf cavity designs that support modes composed of a longitudinally accelerating field in addition to a single transverse multipole, and designs that support modes composed of two transverse multipoles. We discuss generalizing the discoveries and conclusions from the two case studies to designing cavities that support modes composed of any number of multipoles. The theoretical work is verified with analysis of 3D simulations and experimental measurements are presented of a cavity operating in a 3 GHz mode that simultaneously longitudinally accelerates and transversely focuses a beam.

DOI: 10.1103/PhysRevAccelBeams.25.062001

I. INTRODUCTION

The rf cavities that control transverse beam dynamics by operating in transverse magnetic TM_{m10}-like modes composed of a single, dominant transverse multipole of order $m \neq 0$ have a number of applications in particle accelerators. For example, cavities operating in a TM_{110}-like mode with a dominant dipole component in the field have applications in separating a single particle beam into multiple beams [1–3], providing longitudinal diagnostic measurements on a particle beam such as measuring its emittance [4], controlling electron beams in free-electron lasers by acting as emittance exchangers [5], compressing x-ray pulses in synchrotron light sources [6], and providing a head-tail rotation to particle bunches to allow for luminosity control in particle colliders as crab cavities [7]. The latter were investigated at the KEKB collider at KEK [8] with several designs [9] proposed and High-Luminosity LHC (HL-LHC) upgrade at CERN [10]. Additionally, cavities operating in a TM_{210}-like mode with a dominant quadrupolar component are being investigated for application in Landau damping transverse beam instabilities in the HL-LHC [11].

With m, n, and p respectively denoting the azimuthal, radial and longitudinal order of the electromagnetic mode, it is a known and well-studied result that a pillbox cavity, which is an enclosed rf cavity with a circular cross section, will support TM_{mnp}-exact modes with unique resonant frequencies for distinct values of m, n, and p [12]. In order to use an rf cavity that operates in a $m \neq 0$ TM_{mnp} mode in a particle accelerator, novel and elaborate designs [4,13,14] that introduce azimuthal and/or longitudinal asymmetries are required to separate out any degenerate TM_{mnp} same-order modes in frequency space, damp any lower-, same-, and higher-order modes that interfere significantly with beam dynamics, and to optimize the figures of merit such as R/Q. Due to the complexity of such designs, the exact mathematical form of the EM field of the desired mode, and therefore its exact effect on beam dynamics, cannot be solved for analytically. As a result, computationally expensive simulations are required to optimize designs [14,15], and these may be used in tandem with novel mathematical models developed specifically to provide quick but approximate insights into the optimization

*laurence.wroe@physics.ox.ac.uk
†Also at School of Physics, University of Melbourne.

process [16]. Even more, the implementation of azimuthal and longitudinal asymmetries introduces unwanted transverse multipoles into the desired TM_{mnp} mode, and analysis is required to ensure these unwanted multipoles do not exceed tolerance levels for the accelerator's operation [17]. If tolerance levels are exceeded, then this may require a redesign of the rf cavity system: for example, rf cavities that operate in TM_{010}-like modes can be designed with dual-port power couplers instead of single-port couplers to prevent the introduction of unwanted dipolar components [18].

In addition to the application of rf cavities that operate in modes composed of a single multipole, designing rf cavities to operate in modes composed of numerous multipoles could have useful applications in particle accelerators. For example, the use of elliptical irises to introduce transverse quadrupolar focusing in accelerating rf cavities was investigated [19–21] for use in the proposed future linear collider CLIC [22].

In this paper, we present a systematic method for designing rf cavities that support modes composed of any desired number and magnitude of multipolar components. We define these modes with the notation $\mathrm{TM}_{\{M\}\eta p}$. $\{M\}$ denotes the subset of integers representing the multipoles composing the mode: for example, the $\mathrm{TM}_{\{0,1\}\eta p}$ modes are solely composed of a longitudinally accelerating monopolar component and a transverse dipolar component. We use η to denote and distinguish the more complex radial order of general $\mathrm{TM}_{\{M\}\eta p}$ modes from the simpler TM_{mnp} modes, and p continues to denote the longitudinal order of the mode. The method can be applied to modes with any value of p. For simplicity, however, we study the subset of $p = 0$ modes with no longitudinal variation because the vast majority of rf cavities in particle accelerators operate in $p = 0$ modes. The rf cavities that support $\mathrm{TM}_{\{M\}\eta 0}$ modes containing at least two distinct, multipolar components are termed *azimuthally modulated cavities* because we find that the cavity cross section, $r_0(\theta)$, must vary with the azimuth. Such cavities have benefits and application in particle accelerators because the $\mathrm{TM}_{\{M\}\eta 0}$ mode can exactly introduce any number and magnitude of desired multipolar components, is nondegenerate which overcomes the need to separate out a same-order mode in frequency space, and has a field profile that can be expressed analytically throughout the cavity.

Section II begins with the derivation of the transcendental equation that must be numerically solved to determine the azimuthally modulated cross sections that support specific $\mathrm{TM}_{\{M\}\eta 0}$ modes. Insight into the properties of these azimuthally modulated cavity shapes can be gained using mathematical and graphical methods and we first introduce these techniques by applying them to the simple case of the TM_{mn0} modes, known to be supported by cavities with a pillbox shape. We then present two case studies of the azimuthally modulated rf cavity shapes that support the $\mathrm{TM}_{\{0,m_1\}\eta 0}$ modes containing a longitudinally accelerating monopole and a single transverse multipole, and those that support the $\mathrm{TM}_{\{m_1,m_2\}\eta 0}$ modes containing two transverse multipoles. We afterwards discuss generalizing the discoveries and conclusions made in these two case studies for the design of cavity shapes that support modes with any number of multipoles. In Sec. III, we present and analyze simulation results of azimuthally modulated rf cavities designed to support the $\mathrm{TM}_{\{0,3\}\eta 0}$ modes containing a monopolar and a sextupolar component. Finally, in Sec. IV we show the results of experimental bead pull measurements of a novel rf cavity operating in a 3 GHz $\mathrm{TM}_{\{0,2\}20}$ mode.

II. THEORY

A. Deriving the form of a $\mathrm{TM}_{\{M\}\eta 0}$ mode

In this paper, we study perfectly conducting, enclosed rf cavities of longitudinal extent L and cross section $r_0(\theta)$. The modes supported by these azimuthally modulated cavities must have an electric field that satisfies the boundary conditions $E_r(r,\theta,\pm L/2) = E_\theta(r,\theta,\pm L/2) = 0$ at the cavity end points and $E_z(r_0(\theta),\theta,z) = 0$ at the cavity surface. Imposing the former boundary condition and assuming that the particle's transverse momentum is negligible compared to its longitudinal momentum, Panofsky and Wenzel derive that the change in transverse momentum of a particle that passes through an rf cavity can be determined solely by the transverse gradient of the longitudinal component of the electric field, $E_z(r,\theta,z)$ [23]:

$$\Delta\vec{p}_\perp(r,\theta) = -i\frac{q}{\omega}\int_{-L/2}^{L/2}\nabla_\perp E_z(r,\theta,z)dz, \qquad (2.1)$$

where q is the charge of the particle and ω is the resonant angular frequency of the rf cavity mode. The inclusion of the imaginary unit means the transverse force is $\pi/2$ out of phase with the longitudinal force.

The Panofsky-Wenzel theorem therefore states that only the longitudinal electric field of the mode needs to be determined in order to calculate the effect of the transverse forces that act on a particle beam passing through a cavity. The general form of the electric field, $\vec{E}(r,\theta,z)$, of a mode supported by an rf cavity of any design is derived in Ref. [24]. This general form can be simplified to determine the specific form of the longitudinal electric field in azimuthally modulated cavities by applying the boundary conditions at the end points and cavity surface. Applying the end point boundary condition, we find that modes of distinct longitudinal order p must independently satisfy the boundary conditions. Applying the surface boundary condition, we find that the allowed modes belong to one of two familiar sets: either TM modes with no longitudinal magnetic field or TE modes with no longitudinal electric

field. In this paper, we only study TM modes with $p = 0$: TE modes are ignored as they are less frequently used in particle accelerators and their effect on beam dynamics cannot be analyzed using the Panofsky-Wenzel theorem.

The general form of the longitudinal electric field given in Ref. [24] reduces in the case of $\mathrm{TM}_{\{M\}\eta 0}$ modes to

$$E_z(r,\theta,z) = J_0(kr)\tilde{g}_0 + \sum_{m=1}^{\infty} J_m(kr)\tilde{g}_m \cos\,(m\theta - \phi_m), \tag{2.2}$$

where $k = \omega/c$ is the wave number of the mode, $\tilde{g}_m$ and ϕ_m are arbitrary constants that respectively denote the magnitude and offset of the multipole of azimuthal order m, and J_m denotes the Bessel function of the first kind of order m. We note that $\phi_m = 0$ corresponds to a normal multipolar field and $\phi_m = \pi/2$ to a skew multipolar field.

In this paper, the aim is to determine a method for designing rf cavities that support desired modes composed of multipoles of specified magnitudes. If we consider the set of azimuthally modulated cavities with cross sections $r_0^{(\eta)}(\theta)$ that support a desired $\mathrm{TM}_{\{M\}\eta 0}$ mode, then the boundary condition $E_z(r_0^{(\eta)}(\theta),\theta,z) = 0$ must be satisfied at the surface of each of these cavities. Applying this to Eq. (2.2) gives

$$J_0(kr_0^{(\eta)}(\theta))\tilde{g}_0 + \sum_{m=1}^{\infty} J_m(kr_0^{(\eta)}(\theta))\tilde{g}_m \cos\,(m\theta - \phi_m) = 0. \tag{2.3}$$

Equation (2.3) is transcendental and must, in general, be solved using numerical methods to determine $r_0^{(\eta)}(\theta)$. Doing so for user-specified values of k, $\tilde{g}_m$ and ϕ_m returns the set of unique azimuthally modulated cross sections, $r_0^{(\eta)}(\theta)$, that support the corresponding $\mathrm{TM}_{\{M\}\eta 0}$ modes.

B. Modes with a single multipolar component

Although numerical methods must generally be used to solve Eq. (2.3) for all θ, insight into the properties of the azimuthally modulated rf cavities that support $\mathrm{TM}_{\{M\}\eta 0}$ modes can be gained through analysis using mathematical and graphical methods.

To introduce the techniques used for understanding the properties of azimuthally modulated cavities that support modes with more than a single multipole, we briefly analyze the $\mathrm{TM}_{m_1 n 0}$ modes that are known to be supported by a circular pillbox shape [12]. For this case only, Eq. (2.3) can be solved analytically:

$$J_{m_1}(kr_0^{(n)}(\theta))\tilde{g}_{m_1} \cos\,(m_1\theta - \phi_{m_1}) = 0 \tag{2.4}$$

is solved for all θ if

$$J_{m_1}(kr_0^{(n)}(\theta)) = 0 \rightarrow \frac{\omega r_0^{(n)}}{c} = j_{m_1 n}, \tag{2.5}$$

where we define $\phi_0 = 0$ and $j_{m_1 n}$ is the nth root of the Bessel function of order m_1. This shows that the cross section of the cavity that supports a $\mathrm{TM}_{m_1 n 0}$ mode is a circle of constant radius, $r_0^{(n)} = c j_{m_1 n}/\omega$, as expected.

There are a number of important, known results for the $\mathrm{TM}_{m_1 n 0}$ modes [12]. First, because all Bessel functions have $(n-1)$ turning points in the range $[0,\, j_{m_1 n}]$ and the field varies with the azimuth simply as $\cos\,(m_1\theta - \phi_{m_1})$, the integer n is the number of poles (that is minima or maxima) of E_z along any radial line that connects the center of the cavity to its surface, except the nodal lines orientated at $\theta_q = (2q+1)\pi/2m_1 + \phi_{m_1}$ $(q \in \mathbb{Z})$. Second, the $m_1 \neq 0$ modes are degenerate because the boundary condition in Eq. (2.4) is satisfied for all values of ϕ_{m_1}. In contrast, the TM_{0n0} modes are not degenerate. Third, as $j_{m_1 n}$ is unique for all distinct values of m_1 and n, the resonant frequencies of each of the $\mathrm{TM}_{m_1 n 0}$ modes of distinct m_1 and n are unique. Thus to use the TM_{mn0} modes to introduce numerous multipoles at the same frequency, multiple pillbox cavities of different radii would have to be used. Finally, the TM_{010} mode is the fundamental TM_{mnp} mode with the lowest resonant frequency.

We can also use a graphical method to argue that $\mathrm{TM}_{m_1 n 0}$ modes will be supported by cavities with a circular cross section. Considering the 3 GHz TM_{1n0} modes with $\tilde{g}_1 = 1$ and $\phi_1 = 0$, Eq. (2.4) states that the $r_0^{(n)}(\theta_0)$ solutions at a particular angle θ_0 occur where, if plotted as a function of r, $J_1(kr)\cos\theta_0$ intersects the horizontal r axis. Figure 1 plots $J_1(kr)$ (the case where $\theta_0 = 0$) for $r = [0, 25]$ cm. The first three positive intersections with the r axis are indicated by

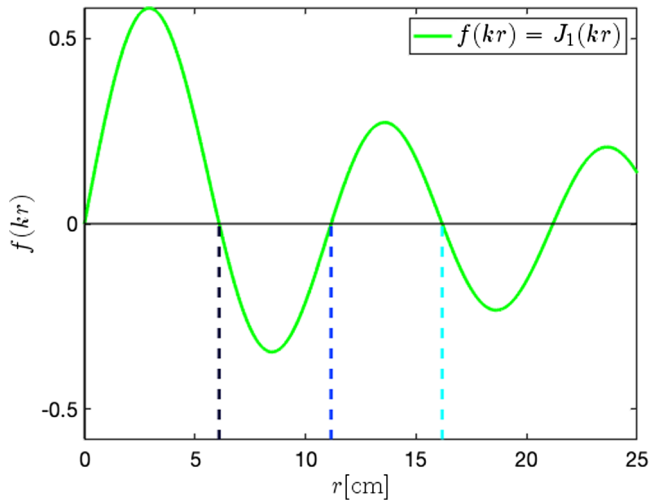

FIG. 1. $J_1(kr)$ plotted against r with $k = 2\pi \times 3$ GHz/c. The black, blue, and cyan dashed lines show three points of intersection with the r axis.

the dashed black, blue, and cyan lines that correspond respectively to the $r^{(n)}(0)$ solutions with $n = 1$, 2, and 3.

We could next consider plotting $J_1(kr)\cos\theta$ for many θ values and determining where the intersections lie for each θ. This is not necessary, however, because the cosine term in $J_1(kr)\cos\theta$ acts as a θ-dependent amplifying term on the Bessel function and thus the locations of the intersections with the r axis will not change. As a result, we conclude that the $r_0^{(n)}(\theta)$ solutions are constant with respect to changes in θ and so plotting any $r_0^{(n)}(\theta)$ solution in Cartesian space plots a circle. This graphical argument can be generalized to argue that $\mathrm{TM}_{m_1 n0}$ modes of any $\tilde{g}_{m_1}$ and ϕ_{m_1} will be supported by a circular pillbox.

C. Modes with a monopolar and a single transverse multipolar component

We now investigate the properties of the $\mathrm{TM}_{\{0,m_1\}\eta 0}$ modes and the corresponding azimuthally modulated cross sections that support them. We begin with general mathematical analysis.

From Eq. (2.2), the subset of $\mathrm{TM}_{\{0,m_1\}\eta 0}$ modes with $\phi_{m_1} = 0$ has a longitudinal electric field of the form:

$$E_z(r,\theta,z) = J_0(kr)\tilde{g}_0 + J_{m_1}(kr)\tilde{g}_{m_1}\cos m_1\theta, \qquad (2.6)$$

and from Eq. (2.3), must satisfy the boundary condition:

$$J_0(kr_0^{(\eta)}(\theta))\tilde{g}_0 + J_{m_1}(kr_0^{(\eta)}(\theta))\tilde{g}_{m_1}\cos m_1\theta = 0. \qquad (2.7)$$

The periodicity of the $\cos m_1\theta$ function in Eq. (2.7) means that both the longitudinal electric field of a $\mathrm{TM}_{\{0,m_1\}\eta 0}$ mode and the corresponding azimuthally modulated cross section have m_1-fold rotational symmetry. Additionally, $r_0^{(\eta)}(0)$ and $r_0^{(\eta)}(\pi/m_1)$ are turning points of opposite forms in the cross section and so if $r_0^{(\eta)}(0)$ is a maximum then $r_0^{(\eta)}(\pi/m_1)$ is a minimum, or vice versa.

Furthermore, if we consider the specific angles $\theta_q = (2q+1)\pi/(2m_1)$ $(q \in \mathbb{Z})$, the cosine term vanishes and Eq. (2.7) becomes

$$J_0(kr_0^{(\eta)}(\theta_q))\tilde{g}_0 = 0 \rightarrow \frac{\omega}{c} r_0^{(\eta)}(\theta_q) = j_{0x}, \qquad (2.8)$$

where $x \in \mathbb{Z}$.[1] As well as relating the cavity frequency and radial value at these angles to the Bessel roots j_{0x}, Eq. (2.8) defines η for the $\mathrm{TM}_{\{0,m_1\}\eta 0}$ modes as the number of poles in E_z specifically along the $\theta_q = (2q+1)\pi/(2m_1)$ radial lines. This can be contrasted with the generality of the interpretation of n as the number of poles in a TM_{mnp} mode along any non-nodal, radial line.

[1]The reason $x \neq \eta$ is due to the possibility of conditional modes, discussed in Sec. II C 2.

As per the TM_{0n0} modes in the circular pillbox cavity, the $\mathrm{TM}_{\{0,m_1\}\eta 0}$ modes supported by azimuthally modulated cavities are also nondegenerate with no same-order mode. Furthermore, by the Courant nodal domain theorem [25], the $\mathrm{TM}_{\{0,m_1\}10}$ modes are the fundamental TM modes in the azimuthally modulated cavities that support them.

Additionally, we note that if the ratio of the transverse multipolar component to the monopolar component is zero, $\tilde{g}_{m_1}/\tilde{g}_0 = 0$, the form of E_z in Eq. (2.6) is equivalent to that of a TM_{0n0} mode. Such modes are supported by a cavity with a circular cross section, as discussed in Sec. II B. The cross section of the cavity that supports a $\mathrm{TM}_{\{0,m_1\}\eta 0}$ mode for a small ratio of transverse multipole to monopole, $\tilde{g}_{m_1}/\tilde{g}_0 \ll 1$, will therefore be perturbed only slightly from circular. Taking the other extreme whereby the transverse multipole to monopole ratio tends to infinity, $\tilde{g}_{m_1}/\tilde{g}_0 \rightarrow \infty$, the cavity cross sections do not tend back to circular but instead tend to unique, noncircular shapes. This asymmetry arises because the $\mathrm{TM}_{m_1 n0}$ modes are degenerate whereas the $\mathrm{TM}_{\{0,m_1\}\eta 0}$ modes are nondegenerate for all ratios of $\tilde{g}_{m_1}/\tilde{g}_0$.

Finally, we consider the azimuthally modulated cross sections that support general $\mathrm{TM}_{\{0,m_1\}\eta 0}$ modes for any value of ϕ_{m_1}. Introducing a $\phi_{m_1} \neq 0$ term into Eqs. (2.6) and (2.7), we find the set of general cavity cross sections are identical to the subset of cavity cross sections with $\phi_{m_1} = 0$, except for a physical rotation about the z axis of ϕ_{m_1}/m_1.

1. Example: Modes with a monopolar and a sextupolar component

It turns out that for certain combinations of m_1 and η, there is a limit on the ratio of transverse multipole to monopole beyond which the cross section of the azimuthally modulated rf cavity becomes discontinuous. This is best illustrated through an example and here we consider 3 GHz $\mathrm{TM}_{\{0,3\}\eta 0}$ modes with $\phi_3 = 0$. Inserting this, $m_1 = 3$ and $k = 2\pi \times 3\ \mathrm{GHz}/c$ into Eq. (2.7) gives the longitudinal electric field profile of such a mode:

$$E_z(r,\theta,z) = J_0(kr)\,\tilde{g}_0 + J_3(kr)\tilde{g}_3\cos 3\theta, \qquad (2.9)$$

and the corresponding cross section can be determined from Eq. (2.7) which we rearrange to

$$J_0(kr_0^{(\eta)}(\theta)) = -\frac{\tilde{g}_3}{\tilde{g}_0} J_3(kr_0^{(\eta)}(\theta))\cos 3\theta. \qquad (2.10)$$

We first solve Eq. (2.10) numerically for a sextupole to monopole ratio of $\tilde{g}_3/\tilde{g}_0 = 0.95$. The cross sections of the rf cavities that support the $\eta = 1$, 2, and 3 modes are plotted in Fig. 2(a). They have threefold rotational symmetry, as expected.

To help understand the properties of these azimuthally modulated cavities, we analyze Eq. (2.10) graphically.

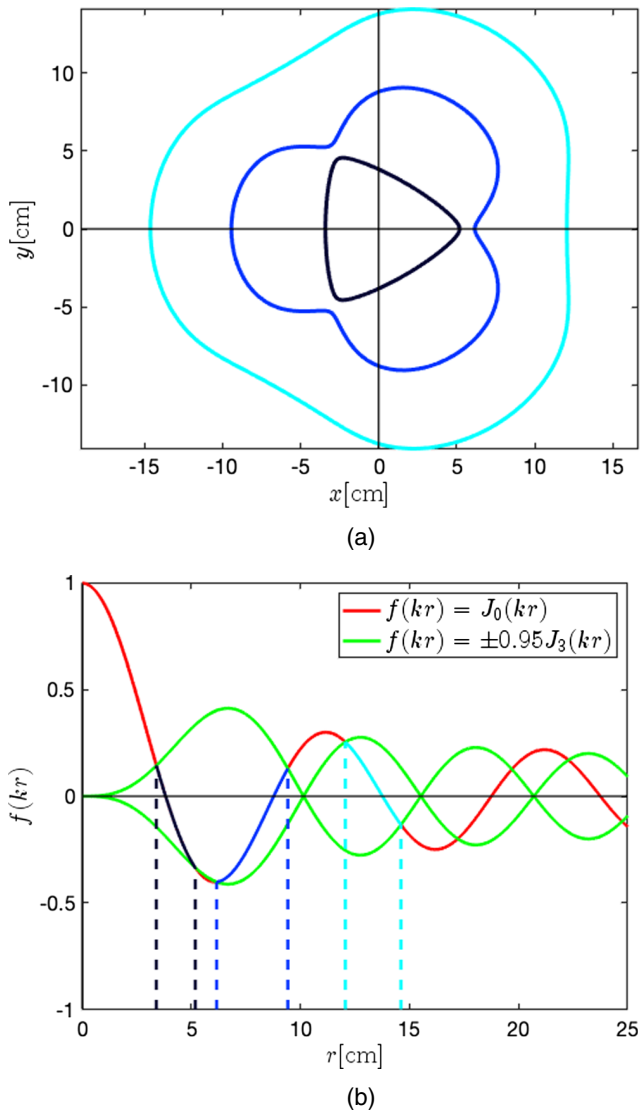

FIG. 2. 3 GHz $\mathrm{TM}_{\{0,3\}\eta 0}$ modes with $\tilde{g}_3/\tilde{g}_0 = 0.95$ and $\phi_3 = 0$. (a) The cavity shapes, $r_0^{(\eta)}(\theta)$, that support the $\eta = 1$, 2, and 3 $\mathrm{TM}_{\{0,3\}\eta 0}$ modes as black, blue, and cyan lines respectively. (b) $J_0(kr)$ and $-0.95J_3(kr)\cos 3\theta$ plotted against r for $\theta = 0$, $\pi/3$. The $\eta = 1$, 2, and 3 solutions where the two functions intersect for all θ are plotted as black, blue, and cyan lines.

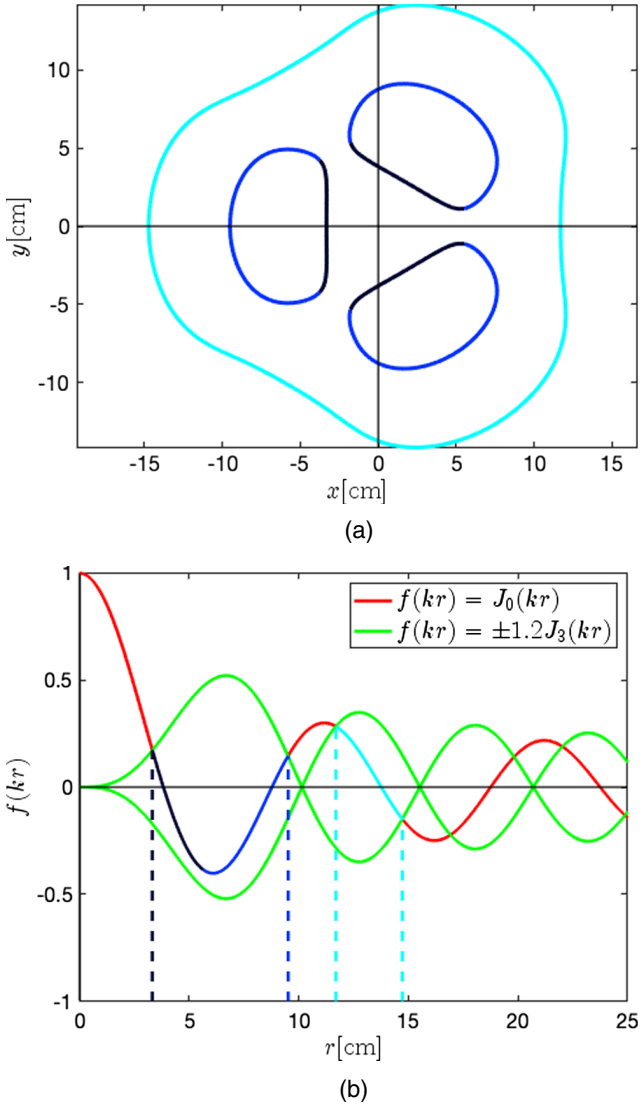

FIG. 3. 3 GHz $\mathrm{TM}_{\{0,3\}\eta 0}$ modes with $\tilde{g}_3/\tilde{g}_0 = 1.2$ and $\phi_3 = 0$. (a) The cavity shapes, $r_0^{(\eta)}(\theta)$, that support the $\eta = 1$, 2, and 3 $\mathrm{TM}_{\{0,3\}\eta 0}$ modes as black, blue, and cyan lines respectively. (b) $J_0(kr)$ and $-1.2J_3(kr)\cos 3\theta$ plotted against r for $\theta = 0$, $\pi/3$. The $\eta = 1$, 2, and 3 solutions where the two functions intersect for all θ are plotted as black, blue, and cyan lines.

Generalizing the monopole term to $J_0(kr)$ and sextupole term to $-0.95J_3(kr)\cos 3\theta$ then, if we plot these two functions against r for a given $\theta = \theta_0$, Eq. (2.10) states the $r^{(\eta)}(\theta_0)$ solutions are the points at which the two functions intersect. Figure 2(b) plots $J_0(kr)$ in red and the two functions $\pm 0.95J_3(kr)$ in green, the latter corresponding to the minimum and maximum values of $\cos 3\theta_0 = \mp 1$. The $\eta = 1$, 2, and 3 points of intersection of the red and green lines are indicated respectively by the black, blue, and cyan vertical dashed lines.

Considering the intersections at other θ values, we note that the monopole term has no θ dependence and thus intersections will always lie on the red, monopolar line for all θ. In contrast, the sextupolar term contains a cosine term that acts as a θ-dependent amplifying term on $-0.95J_3(kr)$. As Fig. 2(b) plots $\pm 0.95J_3(kr)$ which correspond to the maximum and minimum amplification, intersections at all other θ must occur between these maximum and minimum intersections. The solid black, blue, and cyan lines on Fig. 2(b) show the $\eta = 1$, 2, and 3 intersections for all θ and it is clear that each $r^{(\eta)}(\theta)$ solution is bounded between its corresponding vertical dashed lines.

This graphical analysis of Eq. (2.10) in Fig. 2(b) explains why cavity shapes in Fig. 2(a) are physically larger for larger η. Additionally, Fig. 2(b) shows $j_{31} > j_{02}$, that is the third order Bessel function first intersects the r axis after the

zeroth order Bessel has intersected it twice. As a result, both the $\eta = 1$ and $\eta = 2$ cross sections exist in the interval $r = [0, j_{31}]/k \approx [0, 10]$ cm, and this explains why $r_0^{(1)}(0)$ is a maximum whereas $r_0^{(2)}(0)$ is a minimum in Fig. 2(a). This is also why we could not equate η with x in Eq. (2.8) as there may be more than one solution in an interval $r = [j_{m_1(x-1)}, j_{m_1 x}]/k$.

There is a further consequence from having multiple solutions in an interval $r = [j_{m_1(x-1)}, j_{m_1 x}]/k$: if we consider increasing the value of $\tilde{g}_3/\tilde{g}_0$ beyond 0.95 then the $\eta = 1$ and $\eta = 2$ solutions at the angles $\cos 3\theta_0 = 1$ will further converge until, at a critical ratio of $\tilde{g}_3/\tilde{g}_0$, $r_0^{(1)}(\theta_0) = r_0^{(2)}(\theta_0)$. To see this graphically, consider the green line representing $-0.95J_3(kr)$ in Fig. 2(b): if $\tilde{g}_3/\tilde{g}_0$ was increased from 0.95, the $\eta = 1$ (black) and $\eta = 2$ (blue) intersection points at $r \approx 5.5$ cm will move closer together. The critical value at which the $r_0^{(1)}(\theta_0)$ and $r_0^{(2)}(\theta_0)$ converge is numerically calculated as $(\tilde{g}_3/\tilde{g}_0)_{\text{crit}} = 0.98$.

The implication of trying to solve Eq. (2.10) with $\tilde{g}_3/\tilde{g}_0 = 1.2 > (\tilde{g}_3/\tilde{g}_0)_{\text{crit}}$ is shown in Fig. 3: for a range of θ values around $\cos 3\theta = 0$, real $\eta = 1$ and $\eta = 2$ solutions do not exist because there is no intersection between the Bessel terms, and therefore solution, at $r \approx 5.5$ cm. As a result, the $r_0^{(1)}(\theta)$ and $r_0^{(2)}(\theta)$ solutions are discontinuous.

This can be contrasted to the continuous $r_0^{(3)}(\theta)$ solution in Fig. 3(b) whereby the two terms continuously intersect for all θ. In fact, because there is only one root to the zeroth order Bessel function in the interval $[j_{31}, j_{32}]$, the $\eta = 3$ solution is continuous for all values of $\tilde{g}_3/\tilde{g}_0$. We can also see that the $\eta = 3$ solution is bounded within the interval $[j_{31}, j_{32}]/k$, specifically as $\tilde{g}_3/\tilde{g}_0 \to 0$, $r_0^{(3)}(\theta) \to j_{03}/k$, and as $\tilde{g}_3/\tilde{g}_0 \to \infty$, $r_0^{(3)}(\theta) \to [j_{31}/k$ for $\cos 3\theta > 0$; j_{32}/k for $\cos 3\theta < 0]$.

The mathematical solutions to Eq. (2.3) can inform the practical and realistic design of cavities that support $\text{TM}_{\{M\}\eta 0}$-like modes for useful application in particle accelerators. The rf cavities used in particle accelerators must have an enclosed cross section and may have constraints on their maximum physical size and frequency of operation. Therefore, although the $r_0^{(3)}(\theta)$ structure is continuous and enclosed for the multipolar ratio $\tilde{g}_3/\tilde{g}_0 = 1.2$, it is a physically larger cavity than the discontinuous $r_0^{(1)}(\theta)$ and $r_0^{(2)}(\theta)$ shapes. As a potential compromise between creating a mode with the desired $\tilde{g}_3/\tilde{g}_0 = 1.2$ multipolar ratio whilst minimizing the physical size of the cavity that supports it, we can consider designing an rf cavity where the cross section jumps to the $\eta = 3$ solution at the angles where real $\eta = 1$ and $\eta = 2$ solutions do not exist. We define such cavities that mix modes of differing η as *hybrid* cavities and these are further discussed and analyzed in Sec. III.

2. Conditional modes

For the case of the $\text{TM}_{\{0,3\}\eta 0}$ modes, we showed that the $\eta = 1$ and $\eta = 2$ solutions are discontinuous if $\tilde{g}_3/\tilde{g}_0$ exceeds a critical value. This arises because $j_{31} > j_{02}$ and so there are two roots to the zeroth order Bessel function in the interval $[0, j_{31}]$. In contrast, the $\eta = 3$ solution is continuous for all values of $\tilde{g}_3/\tilde{g}_0$ because there is only one root to the zeroth order Bessel function in the interval $[j_{31}, j_{32}]$. Extending this, the azimuthally modulated cavity designed to support a $\text{TM}_{\{0,m_1\}\eta 0}$ mode will have a critical limit on $\tilde{g}_{m_1}/\tilde{g}_0$ beyond which the solution is discontinuous if in the $[j_{m_1(x-1)}, j_{m_1 x}]$ interval in which the $r_0^{(\eta)}(\theta)$ solution lies, there is more than one root to the zeroth order Bessel function.

To generalize this result, we define any $\text{TM}_{\{M\}\eta 0}$ mode of given multipolar content $\{M\}$ and radial order η as *conditional* if any corresponding $r_0^{(\eta)}(\theta)$ solution is discontinuous for any possible combination of magnitudes of the multipolar coefficients. A $\text{TM}_{\{M\}\eta 0}$ mode is therefore *unconditional* if it has a continuous cross section for all possible ratios of the multipolar coefficients.

D. Modes with two different transverse multipolar components

Having determined the properties of azimuthally modulated rf cavities that support the $\text{TM}_{\{0,m_1\}\eta 0}$ modes in the previous subsection, we now examine the azimuthally modulated rf cavities that support the $\text{TM}_{\{m_1,m_2\}\eta 0}$ modes composed of two transverse multipoles.

Using Eq. (2.2), the $\text{TM}_{\{m_1,m_2\}\eta 0}$ modes composed of two different, transverse multipoles with $m_2 > m_1 > 0$ have a longitudinal electric field of the form

$$E_z(r,\theta,z) = J_{m_1}(kr)\tilde{g}_{m_1}\cos(m_1\theta - \phi_{m_1}) + J_{m_2}(kr)\tilde{g}_{m_2}\cos(m_2\theta - \phi_{m_2}). \quad (2.11)$$

Without loss of generality, the corresponding set of azimuthally modulated cavity shapes can be determined from Eq. (2.3) with $\phi_{m_1} = 0$:

$$J_{m_1}(kr_0^{(\eta)}(\theta))\tilde{g}_{m_1}\cos m_1\theta + J_{m_2}(kr_0^{(\eta)}(\theta))\tilde{g}_{m_2}\cos(m_2\theta - \phi_{m_2}) = 0. \quad (2.12)$$

The cross sections that solve Eq. (2.12) and support $\text{TM}_{\{m_1,m_2\}\eta 0}$ modes require further consideration compared to those that support $\text{TM}_{\{0,m_1\}\eta 0}$ modes for four interlinked reasons.

Firstly, solutions do not necessarily have an m_1-fold symmetry but instead a rotational symmetry that varies depending upon the values of m_1, m_2 and ϕ_{m_2}. As a result, η has a more specific definition for $\text{TM}_{\{m_1,m_2\}\eta 0}$ modes.

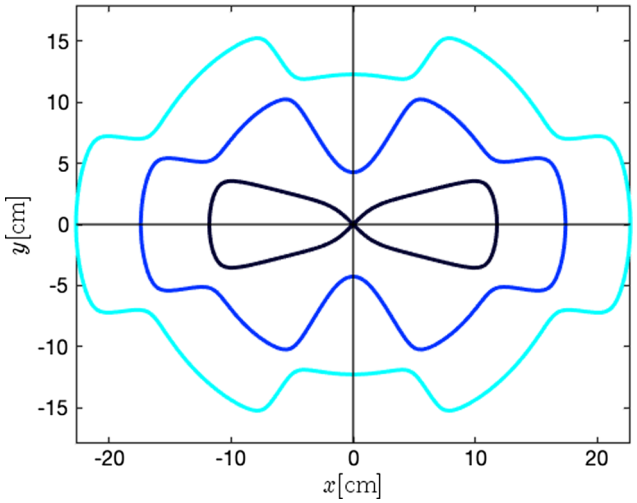

(a)

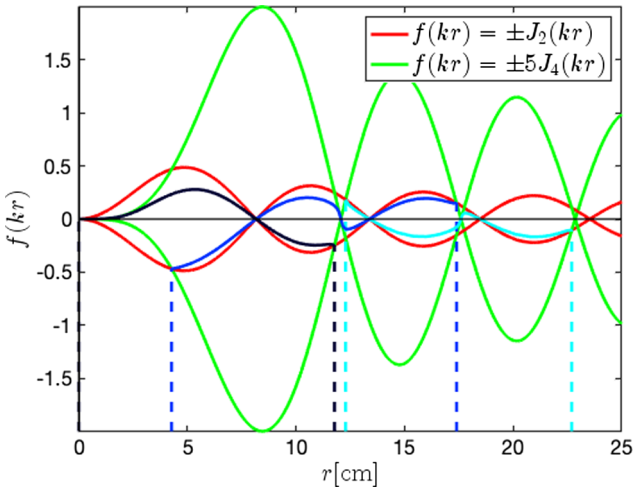

(b)

FIG. 4. 3 GHz $\mathrm{TM}_{\{2,4\}\eta 0}$ modes with $\tilde{g}_4/\tilde{g}_2 = 5$, $\phi_4 = 0$. (a) The cavity shapes, $r_0^{(\eta)}(\theta)$, that support the $\eta = 1$, 2, and 3 $\mathrm{TM}_{\{2,4\}\eta 0}$ modes as black, blue, and cyan lines respectively. (b) $\pm J_2(kr)$ and $\pm 5J_4(kr)$ plotted against r. The $\eta = 1$, 2, and 3 solutions where the $J_2(kr)\cos 2\theta$ and $-5J_4(kr)\cos 4\theta$ functions intersect for all θ are plotted as black, blue, and cyan lines.

Secondly, a practical rf cavity must have $r_0^{(\eta)}(\theta) > 0$, however, $r_0^{(\eta)}(\theta) = 0$ is a valid solution to Eq. (2.12) for all m_1 and m_2. We therefore define a $\mathrm{TM}_{\{m_1,m_2\}\eta 0}$ mode as *forbidden* if $r_0^{(\eta)}(\theta) = 0$ at any angle θ.

Thirdly, solutions are not necessarily bounded within the interval $r = [j_{m_2(x-1)},\ j_{m_2 x}]/k$ due to both terms in Eq. (2.12) having differing orders of cosine dependence.

Fourthly, a practical rf cavity must be closed with $r^{(\eta)}(0) = r^{(\eta)}(2\pi)$, however, solutions of particular m_1, m_2 and ϕ_{m_2} do not satisfy this condition. We define such $\mathrm{TM}_{\{m_1,m_2\}\eta 0}$ modes as *spiral*.

The Appendix derives why certain modes are forbidden or spiral. Section II D 1 presents an example of a forbidden mode and Sec. II D 2 an example of a spiral mode.

$\mathrm{TM}_{\{m_1,m_2\}\eta 0}$ modes can also be conditional whereby the cross section is discontinuous and a hybrid solution needs to be considered if the ratio of the transverse multipolar coefficient of order m_1 to the transverse multipolar coefficient of order m_2 (or vice versa) exceeds a critical value. A $\mathrm{TM}_{\{m_1,m_2\}\eta 0}$ mode will be conditional if, for any $\theta = \theta_0$, there is more than one root to the m_1th order Bessel function within the $[j_{m_2(x-1)}, j_{m_2 x}]/k$ interval that the $r_0^{(\eta)}(\theta_0)$ solution exists in.

1. Example: Modes with a quadrupolar and an octupolar component

To illustrate a forbidden mode, consider the $\eta = 1$, 2, and 3 cross sections that support 3 GHz $\mathrm{TM}_{\{2,4\}\eta 0}$ modes with $\tilde{g}_4/\tilde{g}_2 = 5$ and $\phi_{m_2} = 0$. Numerically solving Eq. (2.12) with these parameters returns the cross sections plotted in Fig. 4(a). Figure 4(b) plots the two Bessel terms for maximum and minimum amplitude and the $\eta = 1$, 2, and 3 solutions. It shows that each solution crosses one interval and so the $\eta = 1$ solution is forbidden. Additionally, because there is only a single root to the second order Bessel function within each $[j_{4(x-1)}, j_{4x}]/k$ interval, all $\mathrm{TM}_{\{2,4\}\eta 0}$ modes are unconditional and each solution bounded between $[j_{4(\eta-2)}, j_{4\eta}]/k$.

2. Example: Modes with a dipolar and sextupolar component

Figure 5 shows an example of a spiral mode by plotting the $r_0^{(\eta)}(\theta)$ solutions in the range $r \approx [0, 15]$ cm that support

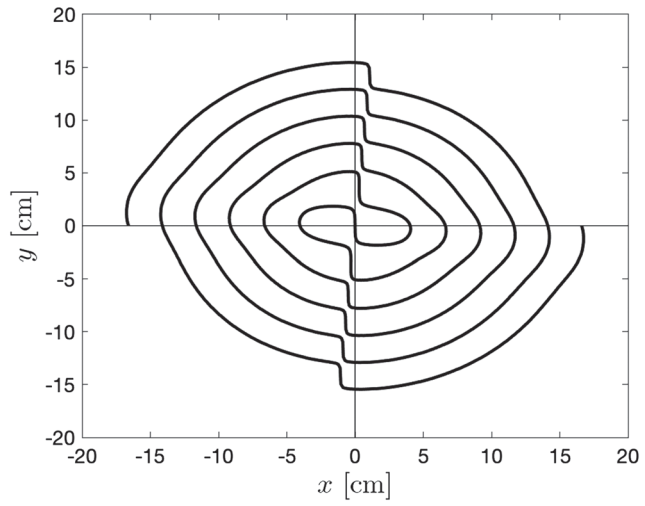

FIG. 5. The $r^{(\eta)}(\theta)$ solutions that support the 3 GHz $\mathrm{TM}_{\{1,3\}\eta 0}$ modes with $\tilde{g}_3/\tilde{g}_1 = 1$ and $\phi_3 = 0.3$ is plotted in black in the range $r \approx [0, 15]$ cm.

3 GHz $\mathrm{TM}_{\{1,3\}\eta 0}$ modes with $\tilde{g}_3/\tilde{g}_1 = 1$ and $\phi_3 = 0.3$. The solutions form a single, continuous, spiralling line which differs from the discrete, closed solutions formed by unconditional solutions of distinct η in previous examples. It is evident that $r_0^{(\eta)}(0) \neq r_0^{(\eta)}(2\pi)$ and therefore this is a spiral mode.

E. Modes with three or more different multipolar components

Equation (2.3) can also be numerically solved to determine the azimuthally modulated cross sections that support $\mathrm{TM}_{\{M\}\eta 0}$ modes with three or more multipolar components. General mathematical analysis of the properties of these modes and the corresponding cross sections that support them is challenging. The concepts of certain modes being conditional, forbidden or spiral, however, generalizes to $\mathrm{TM}_{\{M\}\eta 0}$ modes with any number multipolar content and provides rationale for understanding the numerical solutions to Eq. (2.3) as well as helping to inform the scope and limitation of a general azimuthally modulated rf cavity design.

III. CST SIMULATIONS

Analysis of 3D electromagnetic simulations of azimuthally modulated rf cavities is presented here to confirm the validity of the theoretical work. Electric field distributions, Helmholtz decomposition results, and mode spectra are shown for a pillbox cavity operating in a TM_{310} mode, for azimuthally modulated cavities with continuous cross sections that support the $\mathrm{TM}_{\{0,3\}10}$, $\mathrm{TM}_{\{0,3\}20}$, and $\mathrm{TM}_{\{0,3\}30}$ modes with $\tilde{g}_3/\tilde{g}_0 = 0.95$, and for an azimuthally modulated hybrid cavity that supports a hybrid $\mathrm{TM}_{\{0,3\}10} - \mathrm{TM}_{\{0,3\}30}$ mode with $\tilde{g}_3/\tilde{g}_0 = 1.2$. All modes are normal with $\phi_3 = 0$ and each of the cavities were designed with length 0.5 mm and such that the mode of interest resonates at 3 GHz.

To create the hybrid cavity, the cavity wall is extended from the $r_0^{(1)}(\theta)$ solution to the $r_0^{(3)}(\theta)$ solution at the angles where the $\eta = 1$ solution is no longer real. Although this creates a closed cavity, it introduces additional transverse multipoles into the mode because the boundary condition $E_z(r,\theta,z) = 0$ must also be satisfied where the cavity wall extends from the $\eta = 1$ to the $\eta = 3$ solution. The field is small in this region compared to the field at the center, however, and so the additional multipoles are also small. Thus the hybrid mode is dominantly, but not solely, composed of monopolar and sextupolar components and the cavity will resonate close to, but not exactly at, the designed resonant frequency.

Figure 6 shows the E_z distribution of these different modes. The difference between the TM_{310} mode and $\mathrm{TM}_{\{0,3\}\eta 0}$ modes is evident by comparing the figure parts: there is no longitudinal accelerating field at the center of the circular pillbox cavity operating in the TM_{310} mode [Fig. 6(a)] whereas there is in the case of the $\mathrm{TM}_{\{0,3\}\eta 0}$ modes [Figs. 6(b) and 6(c)]. The resonant frequency of each of the modes was calculated by CST as 3.000 GHz, except for the hybrid cavity which resonated at 3.004 GHz.

Figure 7 shows the multipolar content of each of the five fields calculated using the Helmholtz decomposition method. This method is detailed in Ref. [17] and involves exporting the longitudinal electric field along the surface of cylinders orientated along the cavity axis and then performing an FFT on the data to determine $\tilde{g}_m$. To determine any dependence of these coefficients with radial distance, E_z is exported along 20 discretely formed cylinders of nonlinearly spaced radii in the range [0.02, 0.95] cm. By normalizing the results to $\tilde{g}_3$ in Fig. 7(a), it is clear that the TM_{310} mode in the circular pillbox only contains a sextupole component that is constant with radius. By normalizing the results to $\tilde{g}_0$ in Figs. 7(b)–7(d) we find the calculated multipolar content to be as designed: for example, in Fig. 7(b), $\tilde{g}_0 = 1$ for all radii and $\tilde{g}_3 = 0.95$ for all radii beyond $r \approx 0.03$ cm. The reason for the sextupolar and octupolar components diverging randomly at small r from the expected constant value is because the data must be divided by r^m to determine $\tilde{g}_m$. Simulation errors arising from the finite accuracy of the mesh and numerical errors arising from the pseudo-cylinders being composed only of 360 distinct points are therefore amplified for smaller radii and larger m. Accounting for this error, the multipoles are constant with radial distance for

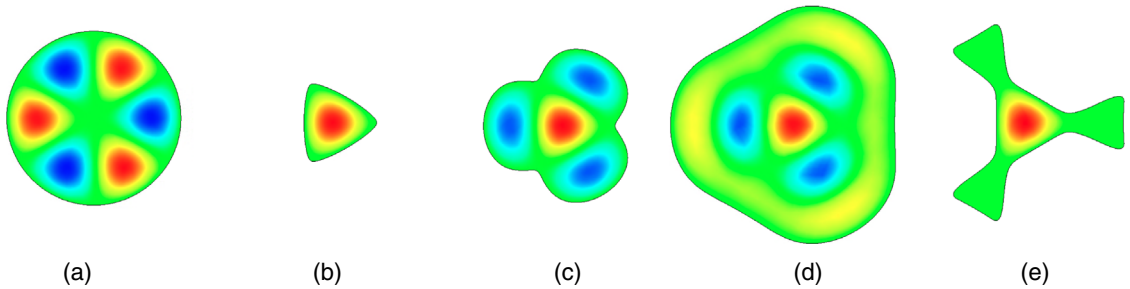

FIG. 6. E_z in cavities operating in 3 GHz TM_{310}, $\mathrm{TM}_{\{0,3\}\eta 0}$ and hybrid $\mathrm{TM}_{\{0,3\}10} - \mathrm{TM}_{\{0,3\}30}$ modes. Red is a maximum in the field, blue a minimum and green is zero. The cavities are to scale: the radius of the circular pillbox is 10.15 cm. (a) TM_{310}. (b) $\mathrm{TM}_{\{0,3\}10}$, $\tilde{g}_3/\tilde{g}_0 = 0.95$. (c) $\mathrm{TM}_{\{0,3\}20}$, $\tilde{g}_3/\tilde{g}_0 = 0.95$. (d) $\mathrm{TM}_{\{0,3\}30}$, $\tilde{g}_3/\tilde{g}_0 = 0.95$. (e) Hybrid TM, $\tilde{g}_3/\tilde{g}_0 = 1.2$.

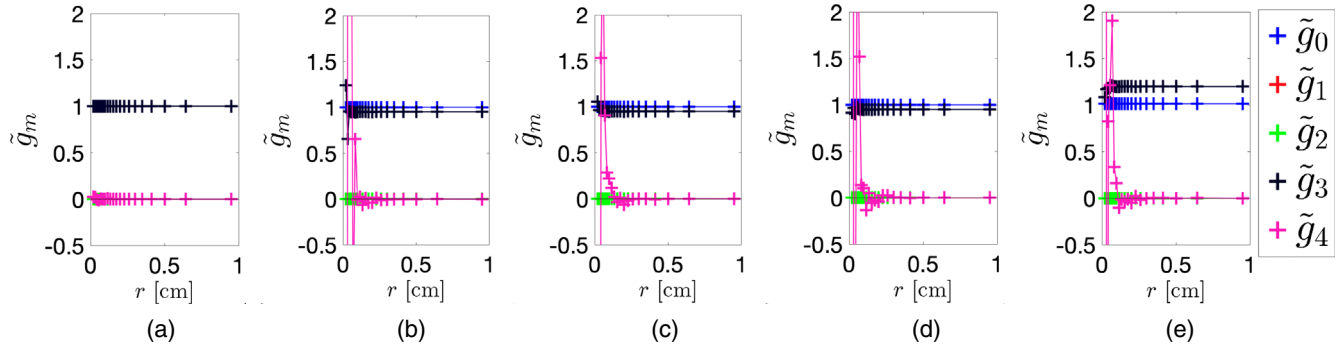

FIG. 7. The calculated multipolar coefficient, $\tilde{g}_m$, is plotted against the distance from the center, r, with color denoting the order, m, for cavities operating in the TM_{310} and four different $\mathrm{TM}_{\{0,3\}\eta 0}$ modes. (a) TM_{310}. (b) $\mathrm{TM}_{\{0,3\}10}$, $\tilde{g}_3/\tilde{g}_0 = 0.95$. (c) $\mathrm{TM}_{\{0,3\}20}$, $\tilde{g}_3/\tilde{g}_0 = 0.95$. (d) $\mathrm{TM}_{\{0,3\}30}$, $\tilde{g}_3/\tilde{g}_0 = 0.95$. (e) $\mathrm{TM}_{\{0,3\}10}$, $\tilde{g}_3/\tilde{g}_0 = 1.2$.

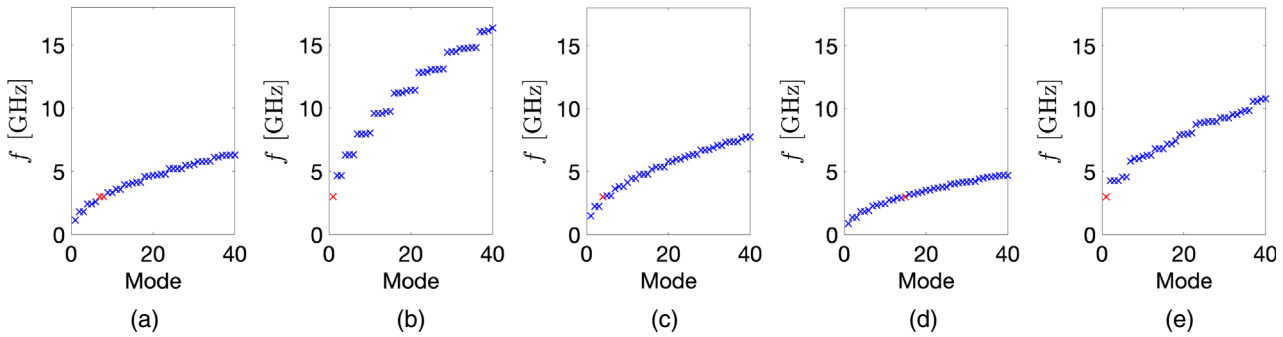

FIG. 8. Frequency spectra of the 40 lowest frequency TM modes for the five different cavity shapes that support the mode denoted in the part caption. The red crosses represent the 3 GHz mode of interest. (a) TM_{310}. (b) $\mathrm{TM}_{\{0,3\}10}$, $\tilde{g}_3/\tilde{g}_0 = 0.95$. (c) $\mathrm{TM}_{\{0,3\}20}$, $\tilde{g}_3/\tilde{g}_0 = 0.95$. (d) $\mathrm{TM}_{\{0,3\}30}$, $\tilde{g}_3/\tilde{g}_0 = 0.95$. (e) $\mathrm{TM}_{\{0,3\}10}$, $\tilde{g}_3/\tilde{g}_0 = 1.2$.

each cavity shape and thus simulation results agree with the radial Bessel dependence given by Eq. (2.2).

The azimuthally modulated rf cavity shapes, $r_0^{(\eta)}(\theta)$, support the infinite number of modes that satisfy their boundary conditions. Figure 8 plots the frequency spectra of the 40 lowest frequency TM modes of the five different cavity shapes. The red crosses denote the 3 GHz mode of interest and any orthogonal degenerate modes of the same frequency. Figure 8(a) shows the TM_{310} mode is not the fundamental but the seventh lowest mode and that it is degenerate with the skew mode, as expected. This can be contrasted with the $\mathrm{TM}_{\{0,3\}10}$ modes in Figs. 8(b) and 8(e): not only are these modes fundamental and nondegenerate, but they also have a larger frequency separation. Additionally, while the frequency spectra of the $\mathrm{TM}_{\{0,3\}20}$ and $\mathrm{TM}_{\{0,3\}30}$ modes is similar in distribution to that of the circular pillbox and the modes are not fundamental, they are evidently nondegenerate with no same-order mode. The frequency spectra of the cavities is important because other modes may require consideration in a particle accelerator if they are excited, directly by the rf power supply or indirectly by a passing beam inducing wakefields, and this significantly interferes with beam dynamics. Any interfering modes may require damping by incorporating lower- and higher-order mode couplers into the design or could necessitate a complete redesign of the cavity.

IV. EXPERIMENTAL TEST OF AN rf CAVITY THAT SIMULTANEOUSLY ACCELERATES LONGITUDINALLY AND FOCUSES TRANSVERSELY

Here in Sec. IV, we show that beam pipes and a dual-port power coupler can be incorporated into an azimuthally modulated rf cavity design whilst maintaining desired multipolar ratios. We also test a prototype in order to verify that the bead pull method can be used to measure the field of an azimuthally modulated cavity and accurately determine the ratio of multipolar terms with minimal error.

A. Designing the cavity

Figure 9 shows the E-field distribution of a critically coupled, single-cell, azimuthally modulated rf cavity system designed to support a 3 GHz $\mathrm{TM}_{\{0,2\}20}$ mode with a quadrupole to monopole ratio of 5.041. Instead of using a single-port coupling system which would introduce a dipolar component into the field of the rf cavity, a dual-port coupling system was used in conjunction with a T-junction waveguide design to split the input power equally into

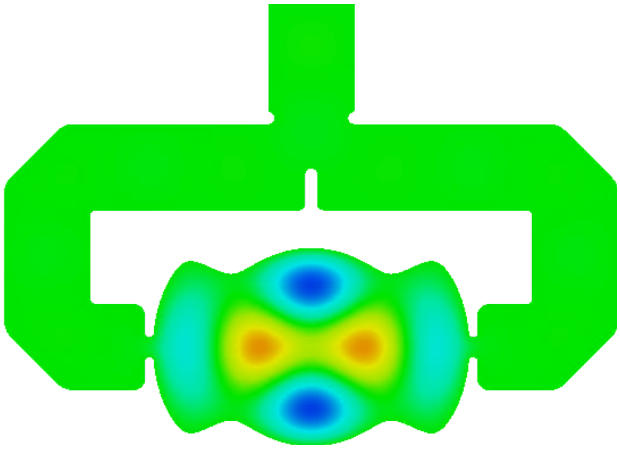

FIG. 9. E_z at the longitudinal center of the designed rf cavity system, where blue is a minimum in the field, orange maximum, and green zero.

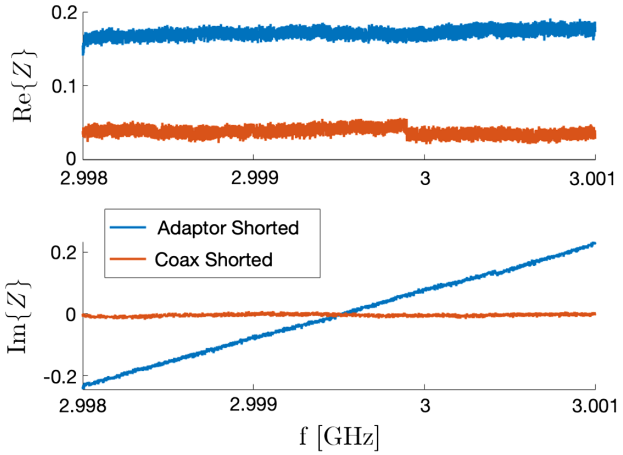

FIG. 11. Impedance measurements of the calibrated coaxial cable shorted, and with the waveguide adaptor attached to the calibrated coax and shorted by clamping an aluminum plate to it.

the two waveguide arms. The dual-port coupler introduces an additional quadrupolar component into the mode. Helmholtz decompositions of simulations showed that by solving Eq. (2.3) for the enclosed rf cavity shape that supports a 3 GHz $\mathrm{TM}_{\{0,2\}20}$ mode with $\tilde{g}_2/\tilde{g}_0 = 4.032$ and $\phi_2 = 0$, and using this shape to create the prototype in Fig. 9 which includes the dual-port coupler and holes at the positions of the poles, the resultant field had a quadrupole to monopole ratio of $\tilde{g}_2/\tilde{g}_0 = 5.041$ and negligible contributions from higher order multipoles. The $\eta = 2$ mode was chosen over the $\eta = 1$ mode in order to give more measurement points to consider and compare.

The rf cavity was designed as two identical halves to be sealed together and was milled out of aluminum. Seven 10 mm diameter holes were drilled into the rf cavity to create holes with centers at the locations of the seven poles in the $\mathrm{TM}_{\{0,2\}20}$ mode. One half the rf cavity system is photographed in Fig. 10.

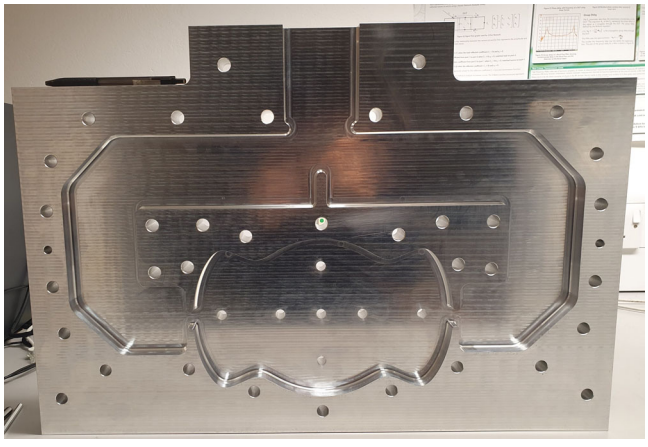

FIG. 10. Half of the rf cavity system designed to support the $\mathrm{TM}_{\{0,2\}20}$ mode with quadrupolar component 5.041 times greater than the monopolar component.

B. Characterization of the rf cavity system

Measurements of the prototype were taken using a vector network analyzer (VNA) connected to a matched waveguide adaptor secured to the top of the cavity waveguide port via coaxial cable. The apparatus was calibrated at the end of the coax, which excluded the matched waveguide adaptor from calibration. To ensure this does not impact results, two cases are compared in Fig. 11: the frequency response of shorting the calibrated coax, and of attaching the waveguide adaptor to the calibrated coax and clamping an aluminum plate to it. The maximum magnitude in the difference of the impedance measurements between the two cases is 0.2 Ω. This is of the order of 100 times smaller than the changes in impedance measured in the bead pull testing and that used for calculating Q-factors. In addition to this, measurements do not give any evidence for resonances in the waveguide adaptor and the external Q-factor does not change significantly between simulations without the waveguide adaptor and measurements with the waveguide adaptor. We thus conclude that the waveguide adaptor's effect on measurements can be neglected.

The resonant frequency of the rf cavity system, f_0, and its intrinsic, Q_0, external, Q_e and loaded, Q_L, Q-factors can be calculated from measurement of the variation in the S-parameter S_{11} with driving frequency and using

$$\beta = \frac{Q_0}{Q_e} = \frac{Q_0 - Q_L}{Q_L} = \frac{1 - S_{11}(f = f_0)}{1 + S_{11}(f = f_0)}, \qquad (4.1)$$

where f is the driving frequency and β is the coupling coefficient. It should be noted that at resonance S_{11} is purely real.

Figure 12 is a Smith chart that shows the measured variation in S_{11} for driving frequencies in the range $f_0 \pm 1$ MHz for five different simulation and experimental measurements. The Smith chart maps the impedance,

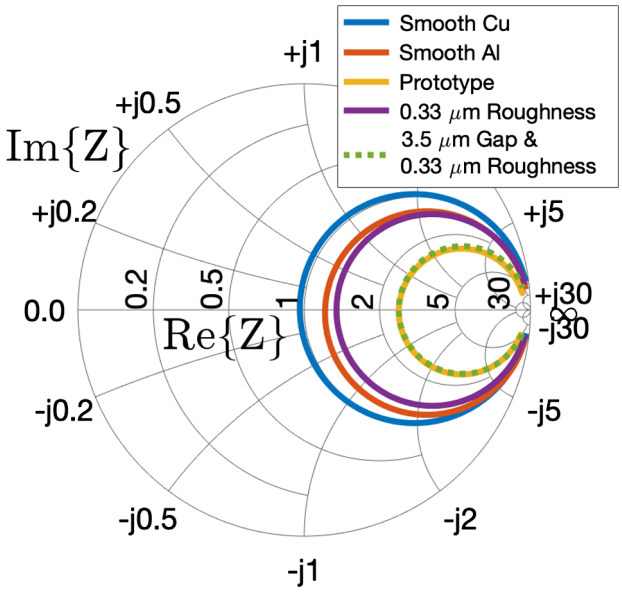

FIG. 12. Smith chart showing the variation in simulation output and experimental measurements of S_{11} in the range $f_0 \pm 1$ MHz.

Z, onto the S_{11} plane and provides a method for visualizing β [26].

The blue line of Fig. 12 represents the simulation output of S_{11} of the rf cavity system modeled as perfectly smooth copper; the electric field from this simulation was shown in Fig. 9. From this data, we calculate $f_0 = 2.99914$ GHz, $Q_0 = 20830$, $Q_e = 20050$ and so the system is critically coupled as $\beta \simeq 1$. The rf cavity coupling ports were optimized for copper, while the prototype was milled out of aluminum to reduce cost. The red line in Fig. 12 shows the simulation output for perfectly smooth aluminum and the impact of the choice of material on β: we calculate $f_0 = 2.99917$ GHz, $Q_0 = 16880$ and $\beta = 0.831$. The yellow line represents the measurement of the prototype, and we calculate that $f_0 = 2.99914$ GHz, $Q_0 = 9120$ and $\beta = 0.410$. The prototype is thus significantly undercoupled compared to the perfectly smooth simulation.

This discrepancy in β is likely due to two effects: first, the surface roughness due to machining of the aluminum which leads to increased resistive losses [27]. The rms surface roughness was measured with a white light interferometer to be 0.33 μm. The purple line shows the simulation output when this level of roughness is included—$f_0 = 2.99955$ GHz, $Q_0 = 15150$ and $\beta = 0.750$. The second effect is rf leakage due to an imperfect seal between the two halves of the prototype. This can be modeled by uniformly separating the two cavity halves: the green dashed line shows that a 0.33 μm surface roughness and 3.5 μm uniform air gap between the two halves replicates the coupling coefficient of experimental measurements—$f_0 = 2.99955$ GHz, $Q_0 = 8490$ and $\beta = 0.410$.

In reality the separation between the two halves of the cavity will not be uniform, however, this would be difficult to model. Simulations show the prototype is particularly sensitive to gaps near the coupling between the waveguide and the cavity and a separation on the order of microns is feasible given the distribution of the bolts used for tightening and the presence of deeper scratches on the aluminum surfaces that are bolted together.

C. Experimental method

Despite the rf cavity system being significantly undercoupled, the electric field of the rf cavity can be determined using the bead pull technique [28–30]. This method uses the result from cavity perturbation theory [31] that when a dielectric bead, small enough such that the EM fields are approximately constant over it, is introduced into an rf cavity at a position (r, θ, z),

$$\Delta f \propto |E_0(r, \theta, z)|^2, \tag{4.2}$$

where Δf is the change in resonant frequency caused by introducing the perturbing object and $E_0(r, \theta, z)$ is the magnitude of the electric field at that position. In our experiments, we used a spherical, plastic bead with a 2.2 mm diameter as the perturbing object.

The VNA cannot be used to measure directly the change in resonant frequency of the rf cavity caused by the perturbing object at a high enough sample rate. An indirect measurement is therefore required. Two possible parameters to use for this indirect measurement are the change in phase of S_{11} or $|\Delta Z|$, where $|\Delta Z| = |Z - Z_{\text{res}}^{\text{unpert}}|$ and $Z_{\text{res}}^{\text{unpert}}$ is the impedance of the unperturbed cavity at the resonant frequency. Figure 13 shows experimental measurements of the variation in $\tan[\arg(S_{11})]$ (top) and $|\Delta Z|$ (bottom) of the unperturbed cavity with f. The dashed lines are linear fits between the respective parameter and f, fitted to and extrapolated from small Δf. The 2.2 mm diameter perturbing bead caused a maximum change in resonant frequency of $|\Delta f| = 0.079$ MHz and the insets of Fig. 13 enlarges this region. It shows $|\Delta Z|$ varies linearly with f to

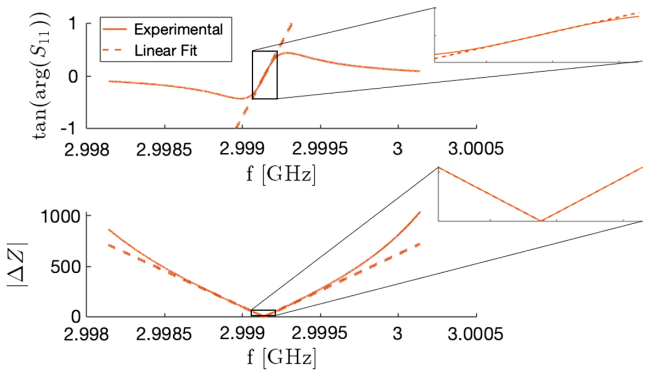

FIG. 13. Measured variation in $\tan[\arg(S_{11})]$ (top) and $|\Delta Z|$ (bottom) with driving frequency. The insets enlarge the region contained inside the black rectangles.

within 0.3%, compared to tan $[\arg(S_{11})]$ which diverges by up to 20%.

We can therefore determine the electric field at a position (r, θ, z) in the rf cavity by measuring, at a fixed driving frequency, the change in impedance caused by the bead at that position and using the relationship

$$|E_0(r, \theta, z)| \propto \sqrt{|\Delta Z|}. \tag{4.3}$$

To carry out a bead pull measurement, we threaded Kevlar wire through one of the holes before centering it using a digital motor system. The 2.2 mm diameter, dielectric bead knotted onto the wire was then pulled through the cavity at a speed of 3 mm/s using a longitudinal motor. The VNA was set up to continuously measure the impedance of the rf cavity at the driving frequency of 2.99914 GHz and sample rate of over 50 points per second. The change in impedance of the rf cavity was measured for the bead being pulled through all seven holes in both longitudinal directions.

D. Experimental results

The data was exported and analyzed in MATLAB [32]. Data collected when the bead was outside the beam pipes, that is $|z| > 38.1$ mm where z is the longitudinal position relative to the center of the rf cavity, was removed from the dataset. A line of best fit between the first and last 50 data points was then used to remove the small linear drift in impedance over time we observed.

Figure 14 compares the longitudinal electric field measurement along each of the seven poles from a CST simulation of the cavity system to the experimental bead pull measurements, where we assume $|E_0| = |E_z|$ for the measurements. Simulation data is plotted as full lines and experimental data as dashed. The different colors

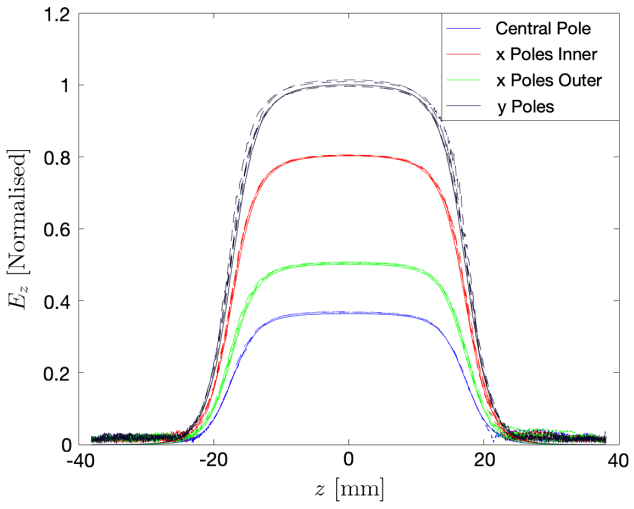

FIG. 14. Comparison of bead pull measurements of the electric field compared to simulation.

TABLE I. Comparison between simulation and experimental measurements of E_z through the different beam pipe locations.

Bead pull along	Simulation	Experimental
y poles	1.000	1.004 ± 0.008
x poles inner	0.802	0.805 ± 0.001
x poles outer	0.501	0.506 ± 0.002
Central pole	0.364	0.368 ± 0.001

correspond to measurements along the different poles: blue denotes the single central pole, red the two inner horizontal (x) poles, green the two outer horizontal (x) poles, and black the two vertical (y) poles. To normalize the simulation data, all data points were divided by the maximum electric field in the y pole. To normalize the experimental data, all data points were divided by the ratio of the mean value of the median experimental electric field measurements between $|z| < 1$ mm along each pole to the mean value of the maximum simulated electric field measurements along each pole. The similarity between experimental and simulation results indicates that the cavity is symmetric in the horizontal, vertical, and longitudinal directions, as expected.

Table I presents a quantitative comparison between the experimental and simulation results with the mean of the electric field measurement between $|z| < 1$ mm shown alongside the standard deviation of the measurements in that range. E_z is expected to be flat in this range with a standard deviation below three decimal places and the results show the experimental data is consistent with simulation. It should be noted that errors arising from inaccuracies aligning the wire to the center of the holes or from divergences from the assumed linearity in Eq. (4.3) have not been included in this analysis.

The data collected thus support that the electric field of the rf cavity is as designed, within error. Therefore we have used successfully the presented theory, in conjunction with 3D simulations to determine the quadrupolar term introduced by the dual-port coupler, to design and measure the field of an azimuthally modulated rf cavity that supports a $\mathrm{TM}_{\{0,2\}20}$ mode with a quadrupolar to monopolar ratio of 5.041.

V. CONCLUSION

This paper has derived the basis of the longitudinal electric fields in azimuthally modulated rf cavities and presented a systematic method for determining the cavity shape that will support $\mathrm{TM}_{\{M\}\eta 0}$ modes. Examples of the rf cavity shapes that support $\mathrm{TM}_{\{0,m_1\}\eta 0}$ or $\mathrm{TM}_{\{m_1,m_2\}\eta 0}$ modes have been explicitly examined with rules derived for rf cavity shapes being conditional, forbidden or spiral depending upon the values of m_1 and η, and m_1, m_2 and η. The theoretical work has been supported by analysis of 3D

simulations and experimental test of an rf cavity that supports a $\mathrm{TM}_{\{0,2\}20}$ mode.

The results of this paper provide a basis for the development of new designs of azimuthally modulated rf cavities that contain any magnitude and order of multipole components. These designs may have useful application in particle accelerators, particularly as they do not have degenerate same-order modes and as they can introduce or cancel wanted or unwanted multipolar components to a fine precision.

Future research can use the formalism and results presented in this paper to guide the development of approximate analytic models of cavity designs and understand how the variation of certain design parameters affects the cavity performance. This could reduce the need to run computationally expensive simulations. Additionally, the paper provides a basis for determining the exact effect of the Bessel dependence of the transverse deflecting fields on beam dynamics. Future studies could also investigate the introduction of longitudinal asymmetries alongside the azimuthal asymmetries in the rf cavity with the aim of enhancing the multipolar content of a field and creating additional parameters with which to optimize performance in aspects such as shunt impedance.

ACKNOWLEDGMENTS

We would like to thank Graeme Burt for many useful discussions and particularly for his assistance in designing the coupler for the rf cavity system. We would also like to thank Shinji Machida, Jean-Baptiste Lagrange, David Kelliher, Chris Rogers and Chris Prior of the ISIS Intense Beams Group for their insightful discussions and feedback, as well as Manjit Dosanjh who has contributed greatly to the direction of the project and regarding the application of discussed work. This study and the experimental work has been funded by the Royal Society under RS\PhD\181200 and RGF\EA\180231, and the CI Core Grant No. ST/P002056/1 has funded travel.

APPENDIX: FORBIDDEN AND SPIRAL MODES

Here we discuss why certain $\mathrm{TM}_{\{m_1,m_2\}\eta 0}$ modes are forbidden, that is $r^{(\eta)}(\theta) = 0$ for some θ value, or spiral, that is $r^{(\eta)}(0) \neq r^{(\eta)}(2\pi)$.

As our first step, we prove that these $r_0^{\eta}(\theta)$ solutions are not necessarily bounded within an interval $r = [j_{m_2(x-1)}, j_{m_2 x}]/k$ ($x \in \mathbb{Z}$). These solutions must solve the boundary condition in Eq. (2.12) that we replicate here:

$$J_{m_1}(kr_0^{(\eta)}(\theta))\tilde{g}_{m_1} \cos m_1\theta + J_{m_2}(kr_0^{(\eta)}(\theta))\tilde{g}_{m_2} \cos(m_2\theta - \phi_{m_2}) = 0. \quad \text{(A1)}$$

First, consider Eq. (A1) for $\theta = 0$: it follows that $r_0^{(\eta)}(0) \neq j_{m_2 y}/k$ ($y \in \mathbb{Z}$). This means that all solutions $r_0^{(\eta)}(0)$ lie within an interval $r = [j_{m_2(x-1)}, j_{m_2 x}]/k$ and not at the limits, or edges, of the interval. Next we consider the unique angles in the range $[0, 2\pi]$, $\theta_q = (2q+1)\pi/2m_1$ ($q = 0, 1, \ldots, \lfloor 2m_1 - 1/2 \rfloor$), which eliminate the cosine term of order m_1 such that Eq. (A1) becomes

$$J_{m_2}(kr_0^{(\eta)}(\theta_q))\tilde{g}_{m_2} \cos\left(\frac{m_2}{m_1}(2q+1)\frac{\pi}{2} - \phi_{m_2}\right) = 0. \quad \text{(A2)}$$

This has two possible solutions whereby either the Bessel term of order m_2 is zero or the cosine term is zero. We will first consider the cosine term to be nonzero, which forces

$$kr_0^{(\eta)}(\theta_q) = j_{m_2 y} \quad \text{(A3)}$$

to satisfy Eq. (A2). Equation (A3) thus states that if $\cos(m_2\theta_q - \phi_{m_2}) \neq 0$, $r_0^{(\eta)}(\theta_q)$ must lie at the limit of an interval $r = [j_{m_2(x-1)}, j_{m_2 x}]/k$. Therefore the solution will cross the upper limit of the interval if the gradient is positive at θ_q, whereas it will cross the lower limit if it is negative. Differentiating Eq. (A1) we find

$$\frac{dr_0^{(\eta)}(\theta)}{d\theta} = \frac{1}{k}\frac{J_{m_1}(kr_0^{(\eta)}(\theta)))\tilde{g}_{m_1} m_1 \sin m_1\theta + J_{m_2}(kr_0^{(\eta)}(\theta))\tilde{g}_{m_2} m_2 \sin(m_2\theta - \phi_{m_2})}{J'_{m_1}(kr_0^{(\eta)}(\theta))\tilde{g}_{m_1} \cos m_1\theta + J'_{m_2}(kr_0^{(\eta)}(\theta))\tilde{g}_{m_2} \cos(m_2\theta - \phi_{m_2})}, \quad \text{(A4)}$$

which if $\cos(m_2\theta_q - \phi_{m_2}) \neq 0$ it becomes

$$\left.\frac{dr_0^{(\eta)}(\theta)}{d\theta}\right|_{\theta_q} = \frac{m_1\tilde{g}_{m_1}}{k\tilde{g}_{m_2}}\frac{J_{m_1}(j_{m_2 y})(-1)^q}{J'_{m_2}(j_{m_2 y})\cos m_2\theta_q} \neq 0. \quad \text{(A5)}$$

Equation (A5) can be numerically evaluated to determine the sign of the gradient at all angles θ_q at the limits of each interval $j_{m_2 y}$. We conclude that if the number of times the gradient is positive does not equal the number of times the gradient is negative (that is the number of times the upper limit of an interval is crossed does not equal the total number of times the lower limit of an interval is crossed) then $r^{(\eta)}(0)$ will lie in a different interval to $r^{(\eta)}(2\pi)$. This means $r^{(\eta)}(0) \neq r^{(\eta)}(2\pi)$ and the solution and mode are spiral. If, however, the number of times the upper limit is crossed equals the number of times the lower limit is crossed, then the solution will lie in the interval $r = [j_{m_2(x-\zeta_1)}, j_{m_2(x+\zeta_2)}]/k$, where the ζ_i are numerically calculated integers. If $\zeta_1 \geq x$

TABLE II. The η values of the first nonforbidden $\mathrm{TM}_{\{m_1,m_2\}\eta 0}$ mode shown for the case $\phi_{m_2} \neq \phi_{m_2}^{(q)}$ (left of comma) and $\phi_{m_2} = \phi_{m_2}^{(q)}$ (right of comma). ∄ denotes a spiral mode.

	m_1								
m_2	1	2	3	4	5	6	7	8	9
2	2, 1	⋯	⋯	⋯	⋯	⋯	⋯	⋯	⋯
3	∄, 1	3, 2	⋯	⋯	⋯	⋯	⋯	⋯	⋯
4	2, 1	2, 1	4, 3	⋯	⋯	⋯	⋯	⋯	⋯
5	∄, 1	3, 2	∄, 2	5, 4	⋯	⋯	⋯	⋯	⋯
6	2, 1	∄, 1	2, 1	3, 2	6, 5	⋯	⋯	⋯	⋯
7	∄, 1	3, 2	∄, 2	3, 2	∄, 3	7, 6	⋯	⋯	⋯
8	2, 1	2, 1	4, 3	2, 2	4, 3	4, 3	8, 7	⋯	⋯
9	∄, 1	3, 2	∄, 1	3, 2	∄, 2	3, 2	∄, 4	9, 8	⋯
10	2, 1	∄, 1	4, 3	3, 2	2, 1	∄, 2	4, 3	5, 4	10, 9

TABLE III. The value of $\phi_{m_2}^{(q)}$ for $\mathrm{TM}_{\{m_1,m_2\}\eta 0}$ modes. O denotes odd integer and N any integer.

	m_1								
m_2	1	2	3	4	5	6	7	8	9
2	$\mathrm{O}\frac{\pi}{2}$	⋯	⋯	⋯	⋯	⋯	⋯	⋯	⋯
3	$\mathrm{N}\pi$	$\mathrm{O}\frac{\pi}{4}$	⋯	⋯	⋯	⋯	⋯	⋯	⋯
4	$\mathrm{O}\frac{\pi}{2}$	$\mathrm{O}\frac{\pi}{2}$	$\mathrm{O}\frac{\pi}{6}$	⋯	⋯	⋯	⋯	⋯	⋯
5	$\mathrm{N}\pi$	$\mathrm{O}\frac{\pi}{4}$	$\mathrm{N}\frac{\pi}{3}$	$\mathrm{O}\frac{\pi}{8}$	⋯	⋯	⋯	⋯	⋯
6	$\mathrm{O}\frac{\pi}{2}$	$\mathrm{N}\pi$	$\mathrm{O}\frac{\pi}{2}$	$\mathrm{O}\frac{\pi}{4}$	$\mathrm{O}\frac{\pi}{10}$	⋯	⋯	⋯	⋯
7	$\mathrm{N}\pi$	$\mathrm{O}\frac{\pi}{4}$	$\mathrm{N}\frac{\pi}{3}$	$\mathrm{O}\frac{\pi}{8}$	$\mathrm{N}\frac{\pi}{5}$	$\mathrm{O}\frac{\pi}{12}$	⋯	⋯	⋯
8	$\mathrm{O}\frac{\pi}{2}$	$\mathrm{O}\frac{\pi}{2}$	$\mathrm{O}\frac{\pi}{6}$	$\mathrm{O}\frac{\pi}{2}$	$\mathrm{O}\frac{\pi}{10}$	$\mathrm{O}\frac{\pi}{6}$	$\mathrm{O}\frac{\pi}{14}$	⋯	⋯
9	$\mathrm{N}\pi$	$\mathrm{O}\frac{\pi}{4}$	$\mathrm{N}\pi$	$\mathrm{O}\frac{\pi}{8}$	$\mathrm{N}\frac{\pi}{5}$	$\mathrm{O}\frac{\pi}{4}$	$\mathrm{N}\frac{\pi}{7}$	$\mathrm{O}\frac{\pi}{16}$	⋯
10	$\mathrm{O}\frac{\pi}{2}$	$\mathrm{N}\pi$	$\mathrm{O}\frac{\pi}{6}$	$\mathrm{O}\frac{\pi}{4}$	$\mathrm{O}\frac{\pi}{2}$	$\mathrm{N}\frac{\pi}{3}$	$\mathrm{O}\frac{\pi}{14}$	$\mathrm{O}\frac{\pi}{8}$	$\mathrm{O}\frac{\pi}{18}$

then the corresponding $\mathrm{TM}_{\{m_1,m_2\}\eta 0}$ mode will be forbidden as it will have $r^{(\eta)}(\theta) = 0$ for some θ.

We now come back to Eq. (A2) and allow the cosine term to be zero. This requires the phase to take one of the following q-dependent values:

$$\phi_{m_2} = \phi_{m_2}^{(q)} = \frac{\pi}{2}\left(\frac{m_2}{m_1}(2q+1) - (2x+1)\right). \tag{A6}$$

The effect of setting the phase term equal to $\phi_{m_2}^{(q)}$ is that at the corresponding θ_q angle, $r_0^{(\eta)}(\theta_q)$ does not lie on the limit of an interval and thus the interval is not crossed.

The work discussed here is brought together in Table II which, for given m_1 and m_2 values between 1 and 10, displays the first nonforbidden and nonspiral mode for $\phi_{m_2} \neq \phi_{m_2}^{(q)}$ (left of comma) and $\phi_{m_2} = \phi_{m_2}^{(q)}$ (right of comma). These were numerically calculated using Eq. (A5). The values of $\phi^{(q)}$ for given m_1 and m_2, as calculated by Eq. (A6), are displayed in Table III.

[1] H. Hahn and H. J. Halama, Design of the deflector for the rf beam separator at the Brookhaven AGS, Rev. Sci. Instrum. **36**, 1788 (1965), 10.1063/1.1719466.

[2] O. H. Altenmueller, R. R. Larsen, and G. A. Loew, Investigations of traveling wave separators for the Stanford Two Mile Linear Accelerator, Rev. Sci. Instrum. **35**, 438 (1964), 10.1063/1.1718840.

[3] A. Citron, G. Dammertz, M. Grundner, L. Husson, R. Lehm, H. Lengeler, D. Plane, and G. Winkler, First operation of a superconducting rf-particle separator, Nucl. Instrum. Methods **155**, 93 (1978).

[4] S. Belomestnykh, I. Bazarov, V. Shemelin, J. Sikora, K. Smolenski, and V. Veshcherevich, Deflecting cavity for beam diagnostics at Cornell ERL Injector, Nucl. Instrum. Methods Phys. Res., Sect. A **614**, 179 (2010).

[5] P. Emma, Z. Huang, K.-J. Kim, and P. Piot, Transverse-to-longitudinal emittance exchange to improve performance of high-gain free-electron lasers, Phys. Rev. ST Accel. Beams **9**, 100702 (2006).

[6] M. Borland, Simulation and analysis of using deflecting cavities to produce short x-ray pulses with the Advanced Photon Source, Phys. Rev. ST Accel. Beams **8**, 074001 (2005).

[7] R. B. Palmer, Energy scaling, crab crossing, and the pair problem, Stanford Linear Accelerator Center Report No. SLAC-PUB-4707, 1988.
[8] Y. Funakoshi (KEKB Commissioning Group), Operational experience with crab cavities at KEKB, in *ICFA miniworkshop on beam-beam effects in hadron colliders*, arXiv:1410.4036.
[9] S. Verdú-Andrés, S. Belomestnykh, I. Ben-Zvi, R. Calaga, Q. Wu, and B. Xiao, Crab cavities for colliders: Past, present and future, in *Proceedings of the 37th International Conference on High Energy Physics (ICHEP)* (Nuclear and Particle Physics Proceedings, Valencia, Spain, 2016), Vol. 273–275, p. 193.
[10] I. Béjar Alonso, O. Brüning, P. Fessia, L. Rossi, L. Tavian, and M. Zerlauth, *High-Luminosity Large Hadron Collider (HL-LHC): Technical design report*, edited by I. Béjar Alonso, CERN Yellow Reports: Monographs (CERN, Geneva, 2020).
[11] A. Grudiev, Radio frequency quadrupole for Landau damping in accelerators, Phys. Rev. Accel. Beams **17**, 011001 (2014).
[12] S. Y. Lee, *Accelerator Physics (Fourth Edition)* (World Scientific, Singapore, 2018), pp. 330–332.
[13] G. Burt, Damping of unwanted modes in SRF deflecting/crabbing cavities, Nucl. Instrum. Methods Phys. Res., Sect. A **734**, 65 (2014).
[14] B. Hall, G. Burt, R. Apsimon, C. J. Lingwood, A. Tutte, A. Grudiev, A. Macpherson, M. Navarro-Tapia, R. Calaga, K. G. Hernández-Chahín, R. B. Appleby, and P. Goudket, Design and testing of a four rod crab cavity for high luminosity LHC, Phys. Rev. Accel. Beams **20**, 012001 (2017).
[15] D. R. Brett, R. B. Appleby, R. De Maria, J. B. Garcia, R. T. Garcia, B. Hall, and G. Burt, Accurate crab cavity modeling for the high luminosity Large Hadron Collider, Phys. Rev. ST Accel. Beams **17**, 104001 (2014).
[16] R. Apsimon and G. Burt, An improved equivalent circuit model of a four rod deflecting cavity, Nucl. Instrum. Methods Phys. Res., Sect. A **847**, 52 (2017).
[17] J. Barranco García, R. De Maria, A. Grudiev, R. Tomás García, R. B. Appleby, and D. R. Brett, Long term dynamics of the high luminosity Large Hadron Collider with crab cavities, Phys. Rev. Accel. Beams **19**, 101003 (2016).
[18] V. Shemelin, S. A. Belomestnykh, R. Geng, M. Liepe, and H. Padamsee, Dipole mode free and kick free 2-cell cavity for the SC ERL Injector, Conf. Proc. C **030512**, 2059 (2003).
[19] W. Schnell, Microwave quadrupoles for linear colliders, CERN Reports No. CERN-LEP-RF-87-24 and No. CLIC-Note-34, 1987.
[20] I. H. Wilson and H. Henke, Transverse focusing strength of CLIC slotted iris accelerating structures, CERN Report No. CLIC-Note-62, 1988.
[21] W. Schnell and I. Wilson, Microwave quadrupole structures for the CERN linear collider, in *Conference Record of the 1991 IEEE Particle Accelerator Conference* (IEEE, San Francisco, US, 1991), Vol. 5, pp. 3237–3239.
[22] M. Aicheler, P. Burrows, M. Draper, T. Garvey, P. Lebrun, K. Peach, N. Phinney, H. Schmickler, D. Schulte, and N. Toge, A multi-TeV linear collider based on CLIC technology: CLIC Conceptual Design Report No. 10.5170/CERN-2012-007, 2012.
[23] W. K. H. Panofsky and W. A. Wenzel, Some considerations concerning the transverse deflection of charged particles in radio-frequency fields, Rev. Sci. Instrum. **27**, 967 (1956).
[24] D. T. Abell, Numerical computation of high-order transfer maps for rf cavities, Phys. Rev. ST Accel. Beams **9**, 052001 (2006).
[25] I. Chavel, *Eigenvalues in Riemannian Geometry* (Academic Press, Orlando, 1984), pp. 19–20.
[26] F. Caspers, rf engineering basic concepts: The Smith chart, arXiv:1201.4068.
[27] S. P. Morgan, Effect of surface roughness on eddy current losses at microwave frequencies, J. Appl. Phys. **20**, 352 (1949), 10.1063/1.1698368.
[28] B. Hall, Designing the four rod crab cavity for the high-luminosity LHC upgrade, Ph.D. thesis, Lancaster University, 2012.
[29] J. Shi, A. Grudiev, and W. Wuensch, Tuning of X-band traveling-wave accelerating structures, Nucl. Instrum. Methods Phys. Res., Sect. A **704**, 14 (2013).
[30] I. V. Konoplev, K. Metodiev, A. J. Lancaster, G. Burt, R. Ainsworth, and A. Seryi, Experimental studies of 7-cell dual axis asymmetric cavity for energy recovery linac, Phys. Rev. Accel. Beams **20**, 103501 (2017).
[31] J. C. Slater, Microwave electronics, Rev. Mod. Phys. **18**, 441 (1946).
[32] MATLAB Version 9.3.0.713579 (R2020a) (The Mathworks, Inc., Natick, Massachusetts, 2020).

Correction: A proof inquiry was misinterpreted during the production cycle, resulting in publication of text errors in the second and fourth paragraphs of Sec. I. These errors have been fixed.